PAPER

Check for updates

ZnO@ZIF-8 core–shell heterostructures with improved photocatalytic activity†

Mei-Hua Chen, Qian-Ying Lu, Yi-Ming Li, [ID]* Ming-Ming Chu* and Xue-Bo Cao*

ZnO semiconductors have been widely used as photocatalysts. However, the weak photodegradation under solar light restrains their further application. In this study, porous zeolitic imidazolate framework-8 (ZIF-8), which has a high specific surface, was combined with ZnO nanorods to fabricate ZnO@ZIF-8 core–shell heterostructures, with the ZnO nanorods and ZIF-8 as the core and the shell, respectively. Scanning electron microscopy and transmission electron microscopy measurements revealed that the ZnO nanorods were wrapped by a ZIF-8 shell. The pore size distribution of these ZnO@ZIF-8 nanocomposites included micropores, mesopores, and macropores. Moreover, a Brunauer–Emmett–Teller analysis showed an increase compared with the ZnO nanorods in the overall specific surface area. Due to a synergistic effect of ZnO and ZIF-8, the as-synthesized ZnO@ZIF-8 heterostructures exhibited high photocatalytic activity and completely degraded methylene blue in ~4.5 min under solar light irradiation. Furthermore, stability experiments proved that the as-prepared ZnO@ZIF-8 nanocomposites retain over 95% of their photocatalytic activity after four cycles.

Introduction

The application of photocatalytic technology in the treatment of refractory organic wastewater and comprehensive wastewater has attracted considerable attention due to its high catalytic activity, simple equipment, convenient operation, low energy consumption, strong oxidation capacity, and no secondary pollution.[1,2] Semiconductors are among the most effective photocatalysts.[3] The semiconductor photocatalysts presently studied are mostly N-type semiconductors with a wide bandgap. Among them, TiO_2 and ZnO possess the highest catalytic activity and have been widely applied in photocatalytic degradation because of their unique electronic structure, non-toxicity, and environmentally friendly nature.[3–6] To date, some studies have shown that ZnO semiconductors with abundant nanoscale morphologies (*e.g.*, nanorods, nanobelts, nanotetrapods, nanoflowers, and nanopyramids) are more effective than the TiO_2 ones in the photocatalytic treatment of some refractory organic pollutants in wastewater.[7,8] However, their application has two great restrictions. The wide bandgap of ZnO limited the absorption to the ultraviolet (UV) radiation,[3] and the rapid recombination of electron–hole pairs, which results in

photocatalytic activity degradation. Nonetheless, morphology control,[9,10] element doping,[11–13] semiconductor coupling,[14,15] and heterojunction construction[16,17] can effectively enhance the photocatalytic properties of ZnO semiconductors. ZnO nanocomposites with special core–shell heterostructures have attracted tremendous attention due to their easily controllable structures, morphologies, and functions.[18–21]

Metal–organic frameworks (MOFs) are crystalline inorganic–organic hybrid materials.[22] Because of their high thermal stability, chemical stability, and adjustable structure and function,[23–25] much attention has been paid to the potential applications of MOFs in gas adsorption and separation, ion exchange, chemical catalysis, gas storage, and other fields.[26–29] Zeolitic imidazolate framework-8 (ZIF-8), a MOF composed of Zn^{2+} in tetrahedral coordination with four 2-methylimidazole (2-Melm) ligands, is a photocatalyst that can be used to degrade organic pollutants under UV irradiation.[30] ZnO@ZIF-8 core–shell heterostructures have been reported in many studies.[18,19,31–36] As regards photodegradation, Zhan *et al.*[34] used a self-template strategy to prepare ZnO@ZIF-8 nanorods by using a water–dimethylformamide solution. Yu *et al.*[35] studied the degradation effect of ZnO@ZIF-8 nanospheres on methylene blue (MB). Wang *et al.*[19] achieved selective reduction of Cr(VI) in a Cr(VI)–MB solution due to the size selectivity of ZIF-8 in ZnO@ZIF-8 heterostructures. Tuncel *et al.*[36] attributed the enhanced adsorption capacity and photoactivity of such nanocomposites to the high surface area and porous structure of ZIF-8. Although the photocatalytic performance

College of Biological, Chemical Sciences and Engineering, Jiaxing University, Jiaxing, 314001, China. E-mail: liyiming@zjxu.edu.cn, chumingming@zjxu.edu.cn, xbcao@zjxu.edu.cn
† Electronic supplementary information (ESI) available. See DOI: 10.1039/d1ce00559f

of ZnO@ZIF-8 nanocomposites has been optimized and improved so far,[19,34,35] the photodegradation performance of ZnO cannot be significantly improved under solar light irradiation.

In the present study, ZnO nanorods were used as self-sacrificing templates to fabricate ZnO@ZIF-8 core–shell heterostructures with ZnO nanorods and ZIF-8 as the core and shell, respectively. The as-synthesized ZnO@ZIF-8 core–shell nanorods had a diameter of 10–20 nm and a shell thickness of ~3 nm. Experimental results showed that the photocatalytic activity of the prepared ZnO@ZIF-8 nanorods was twice as high as that of ZnO nanorods, confirming the improvement by the combination with ZIF-8. Besides, these nanocomposites achieved complete MB photodegradation within only 4.5 min under solar light irradiation, which is significantly higher than that of the similar composites reported. Furthermore, they exhibited high stability, retaining over 95% of their photocatalytic activity after four cycles.

Experimental

Chemicals

Zinc nitrate hexahydrate (99.0%), 2-methylimidazole (98.0%), and methanol (≥99.5%) were purchased from SAAN Chemical Technology Co., Ltd. (Shanghai, China). Zinc acetate (99%) and potassium hydroxide were provided by Aladdin Reagent Co., Ltd. (Shanghai, China). All the reagents were of analytical grade purity and used without further purification.

Preparation of ZnO@ZIF-8 core–shell heterostructures

First, ZnO nanorods were synthesized according to a previously published procedure[37] as follows. Zinc acetate (14.8 g) and potassium hydroxide (7.4 g) were dissolved in 60 and 32 mL of methanol, respectively. Their resulting solutions were mixed and stirred for 72 h at 70 °C. Then, the as-formed ZnO nanorods were separated from the solution *via* centrifugation, washed repetitively with methanol and distilled water several times, and freeze-dried.

Then, ZIF-8 was grown on these ZnO nanorods with a simple solvothermal method as follows. 2-MeIm (20 mL, 2.0 mg mL^{-1} in methanol solution) and the ZnO nanorod powder (0.3 g) were sequentially added to a 50 mL Teflon-lined stainless-steel autoclave. After sonication for 3 min, the autoclave was transferred to an oven preheated to 80 °C. After the mixture reacted for 24 h, the resulting white product was collected *via* centrifugation and washed repetitively with methanol and distilled water several times. Finally, the ZnO@ZIF-8 core–shell nanorod powder was obtained after freeze-drying.

Structural characterization

The morphology and structure of the ZnO and ZnO@ZIF-8 nanorods were analyzed using a scanning electron microscopy system (Hitachi S-4800, Hitachi Ltd.) and a transmission electron microscopy (TEM) instrument (FEI Tecnai G20, FEI Company). Powder X-ray diffraction (XRD) spectra were recorded with a Bruker D8 FOCUS powder X-ray diffractometer (Gemini E, Agilent Technologies Co. Ltd.) using Cu Kα radiation (40 kV, 40 mA). Nitrogen sorption analysis was conducted using a TriStar 3020 and an ASAP 2020 analyzer (Micromeritics Instrument Co.) at 77 K, and the specific surface area was calculated *via* the Brunauer–Emmett–Teller (BET) method. The MB solution absorbance was measured using a UV-vis spectrophotometer (UV-1100, Shanghai Meipinda Instrument Co., Ltd) at 664 nm, which is the maximum absorption wavelength of MB. UV-vis absorption spectra of the as-prepared ZnO and ZnO@ZIF-8 nanorods were recorded with a UV-vis near infrared spectrophotometer (Cary 5000, Agilent Technologies Co. Ltd.). The electrochemical impedance spectroscopy (EIS) and
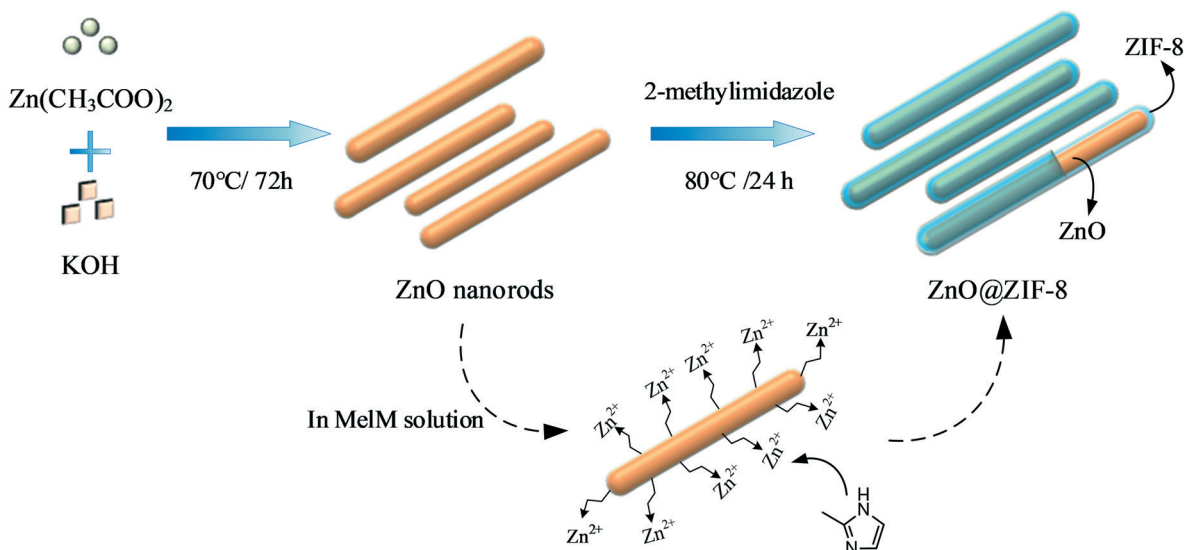

Fig. 1 Growth process of ZnO@ZIF-8 core–shell nanorods.

transient photocurrent response curves were acquired with a three-electrode system using an electrochemical workstation (CHI 760E, Shanghai Chenhua Instrument Co. Ltd.), and a 300 W xenon lamp (CEL HXF300, Aulight Beijing).

Photoelectrochemical measurements

The photocatalytic activities of the as-prepared photocatalysts were evaluated according to their photodegradation of an MB solution under solar light. The nanocomposites (50 mg) were mixed with 50 mL of 1.0×10^{-5} mol L^{-1} MB solution (3.19 mg L^{-1}) under magnetic stirring for 30 min in the dark to uniformly disperse the photocatalyst powder. Afterward, the mixture was exposed to solar light to test the photocatalytic performance. Meanwhile, to measure the absorbance, 1 mL of the liquid part was collected from the mixed solution at definite times with a syringe and filtered using a microporous membrane (0.22 μm). The progress of the photocatalytic degradation of MB in an aqueous solution was calculated as follows.

$$C/C_0 = A/A_0, \tag{1}$$

where C_0 (in mg mL^{-1}) and C (in mg mL^{-1}) are the initial and real-time MB concentrations of the solution, respectively, and A_0 and A are their initial and real-time absorbance, correspondingly.

Then, to test the photocatalytic stability, the photocatalysts were recollected by centrifugation and redispersed in the same MB aqueous solution for the next cycle, and the other experimental parameters were the same as in the first cycle.

Results and discussion

Preparation and physico-chemical characterization

ZnO is an amphoteric metal oxide that releases a small amount of Zn^{2+} when mixed with basic or acidic solutions.[19] As shown in Fig. 1, a small amount of Zn^{2+} was gradually dissolved from the synthesized ZnO nanorods into the 2-Melm solution, which possessed weak alkalinity with a pK_a value of 14.2.[19] Then, the 2-Melm molecules reacted with Zn^{2+}, forming ZIF-8 that deposited on the surface of the ZnO nanorods. Thus, when preparing the ZnO@ZIF-8 core–shell nanocomposites, the ZnO core not only acted as a carrier but also provided a zinc source to form the ZIF-8 shell. ZIF-8 was left to grow over time until the ZnO nanorods were completely wrapped.

The ZnO nanorods were prepared by refluxing zinc acetate with potassium hydroxide, both in methanol solutions, for 3 days. As shown in Fig. 2a, the morphology of the synthesized ZnO nanorods was regular and uniform, with a diameter of 10–20 nm and a length of ~100 nm. Besides, there were no other ZnO morphologies and the dispersion was good. The ZnO@ZIF-8 nanocomposites (Fig. 2b and c) showed the same morphology as the original ZnO nanorods. The TEM analysis (Fig. 2d), performed to investigate the inner structure of the
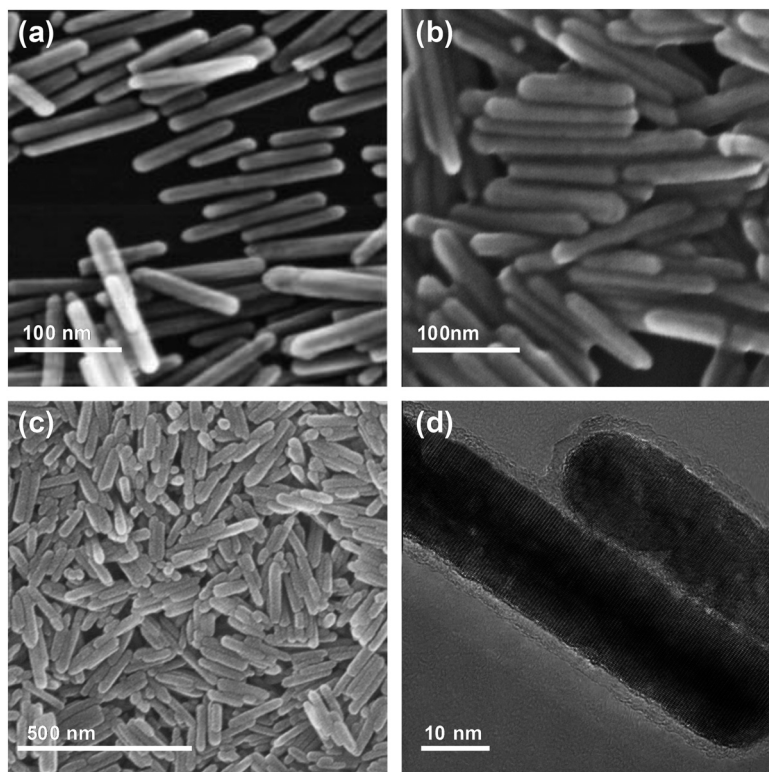

Fig. 2 (a) Scanning electron microscopy (SEM) image of ZnO nanorods. (b) SEM image of ZnO@ZIF-8 in solution. (c) SEM image of ZnO@ZIF-8 after freeze-drying. (d) Transmission electron microscopy (TFM) image of ZnO@ZIF-8.

ZnO@ZIF-8 nanocomposites, revealed that the ZnO nanorods were covered by a ~3 nm-thick layer of ZIF-8 crystal polyhedra, confirming the production of ZnO@ZIF-8 core–shell heterostructures.

The mineralogical composition of the products was identified *via* XRD. As shown in Fig. 3a, the ZnO@ZIF-8 nanorods exhibited diffraction peaks at 7.3°, 10.3°, 12.6°, and 18.0° belonging to the (011), (002), (112), and (222) crystal planes of the zeolitic structure of ZIF-8, as well as signals at 31.8°, 34.5°, 36.4°, 47.7°, and 56.6° attributed to the (100), (002), (101), (102), and (110) crystal planes of the hexagonal wurtzite structure of ZnO (JCPDS No. 36-1451). Besides, the ZIF-8 diffraction peaks were relatively weak compared with the ZnO ones, further confirming that the thickness of the ZIF-8 shell was relatively thin.

Effect of the 2-Melm concentration

It is noted that the 2-Melm concentration can influence the morphology and photodegradation performance of the synthesized nanocomposites.[19,34] Hence, the ZnO@ZIF-8 nanorods were prepared using methanol solutions with various 2-Melm concentrations (2, 5, and 10 mg mL^{-1}). As shown in Fig. S1a,† when the 2-Melm concentration was 2 mg mL^{-1}, the resulting products consisted of only the independent ZnO@ZIF-8 core–shell heterostructures. When the 2-Melm concentration was increased to 5 mg mL^{-1} (Fig. S1b†), some nanogranular materials also appeared among the products. At the highest 2-Melm concentration tested (Fig. S1c†), there were more granular materials and some of them wrapped the nanorods. This can be explained as follows. In theory, one Zn^{2+} ion should coordinate with two 2-Melm molecules.[19] Zhan *et al.*[34] pointed out that the balance between the dissolution rate of Zn^{2+} and its coordination rate with 2-Melm is crucial for the formation of ZnO@ZIF-8 nanorods. Increasing the 2-Melm concentration would improve both these parameters.[34] Thus, when the 2-Melm concentration is low, the dissolution rate of Zn^{2+}

from the ZnO nanorods is relatively mild, giving the 2-Melm molecules enough time to coordinate with Zn^{2+} on the nanorod surface. This is why, when the 2-Melm concentration was 2 mg mL^{-1}, the ZnO nanorods were completely covered by ZIF-8 and the ZnO@ZIF-8 nanocomposites were the only products (Fig. S1a†). In contrast, when the 2-Melm concentration is high, Zn^{2+} would dissolve quickly from ZnO, diffusing into the solution. Then, some 2-Melm molecules would coordinate with Zn^{2+} near the surface of the ZnO nanorods to form the ZnO@ZIF-8 nanocomposites while others would coordinate with the diffused Zn ions to form separate ZIF-8 nanoparticles.

Fig. 3b shows the XRD patterns of the ZnO@ZIF-8 nanocomposites prepared using the various 2-Melm concentrations tested, showing an increase in the intensity of the diffraction peaks (7.3°, 10.3°, 12.6°, and 18.0°) corresponding to the zeolitic structure of ZIF-8 along with the 2-Melm concentration. This further proves that varying the 2-Melm concentration can lead to an increase in the ZIF-8 shell thickness or a formation of ZIF-8 monomers.

BET analysis

The specific surface area of a photocatalyst has a direct and significant effect on its photocatalytic activity.[9] In general, when a semiconductor is excited by light irradiation with an energy equal to or higher than its bandgap energy, a certain number of electrons in the valence band migrate into the conduction band (CB), leaving the valence band (VB) with an equal number of holes. Then, these electrons and holes are transferred to the semiconductor surface and react with O$_2$ and OH$^-$ in water, forming active groups with strong oxidation ability. Finally, these active groups react with and decompose the organic pollutants adsorbed on the semiconductor surface.[3,38]

The specific surface areas of the synthesized ZnO and ZnO@ZIF-8 nanorods were measured *via* the nitrogen adsorption–desorption technique (Fig. 4). According to the
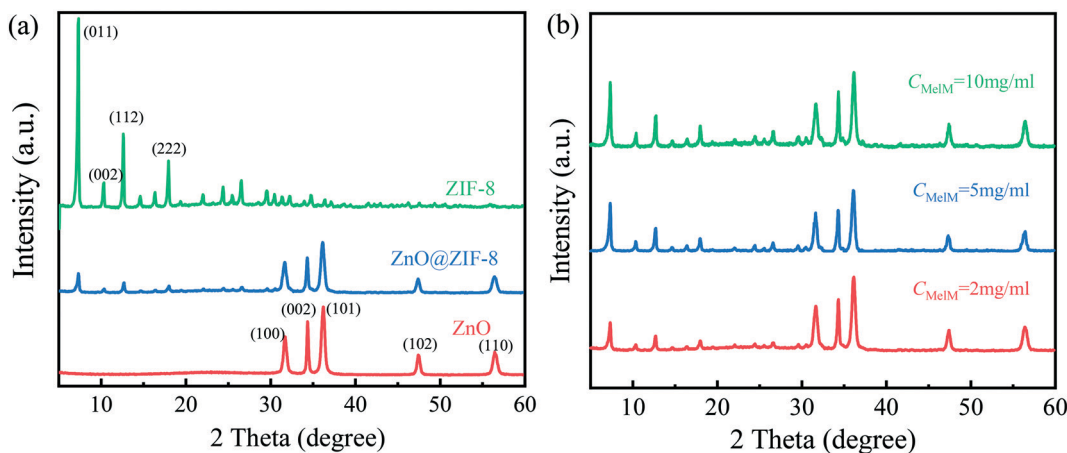

Fig. 3 (a) X-ray diffraction (XRD) patterns of ZIF-8, ZnO nanorods, and ZnO@ZIF-8 core–shell nanorods. (b) XRD patterns of ZnO@ZIF-8 core–shell nanorods prepared using 2-methylimidazole (2-Melm) concentrations of 2, 5, and 10 mg mL^{-1}.
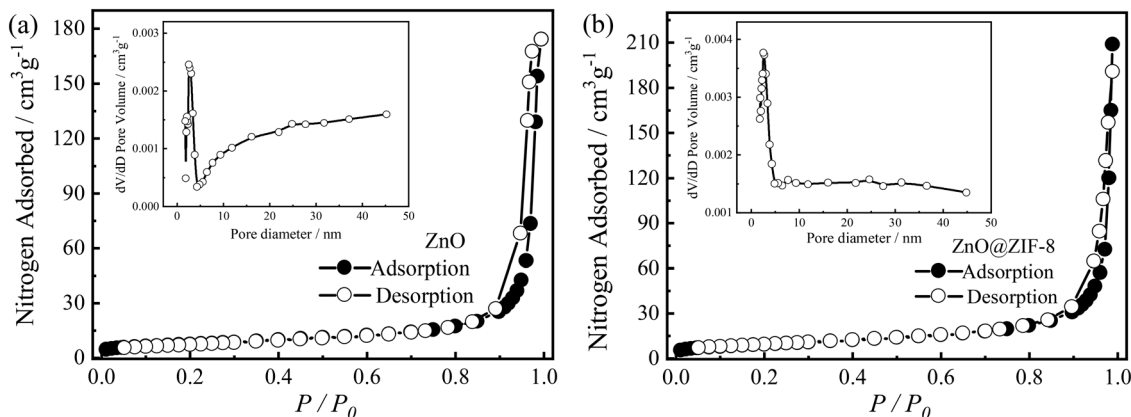
Fig. 4 Nitrogen adsorption–desorption isotherms of (a) ZnO and (b) ZnO@ZIF-8 core–shell nanorods. The insets show the corresponding pore size distributions.

BET results, the ZnO nanorods had a specific surface area of 55.6 m^2 g^{-1}, with the pore size distribution ranging from micropores to macropores. The formation of these pores could be attributed to the accumulation of ZnO nanorods since these micropores were larger than those of the ZnO nanorod ones, probably due to the porosity of ZIF-8, whose pore diameters were mainly micropores of ~2 nm.

Photocatalytic activity

The dark adsorption experiment was carried out to test the adsorption effect of MB. As shown in Fig. S2,† the samples reached adsorption equilibrium in almost 30 min, and ZnO@ZIF-8 shows better adsorption performance than ZnO. The adsorption of ZnO and ZnO@ZIF-8 is 14.5% and 30.1% respectively, which is agreement with the specific surface area of the samples and the performance reported in the literature.[36,39]

The photocatalytic performances of the ZnO and ZnO@ZIF-8 nanorods were evaluated *via* MB degradation under solar light irradiation. Fig. 5a and S3a and b† show the time-dependent UV-vis absorption spectra of MB solutions treated with ZnO@ZIF-8 core–shell nanocomposites, ZnO nanorods, and ZIF-8 as photocatalysts. When increasing the photodegradation time, the maximum absorbance peak of the MB solution (at 664 nm) was reduced significantly in all cases, confirming the gradual photocatalytic degradation of MB. However, the catalytic activity of ZIF-8 was quite poor, and it could not completely degrade MB even when the reaction time reached 120 min.

Fig. 5b and S3c† show the photocatalytic degradation of MB in aqueous solutions. It can be seen that MB would be hardly degraded in the absence of any catalyst under solar light. The photocatalytic activity of ZnO is pretty good which could mainly be attributed to its high crystallinity and high dispersion.[37,40] Besides, the photosensitization of MB molecules to the surface of ZnO is an important factor to improve its solar light degradation performance. The MB molecule adsorbs photons to produce a photogenerated electron, which is injected into the conduction band of ZnO, and produce super oxide radicals (Fig. S6c†), leading to the degradation of MB in the solution.[41,42]

When using the synthesized ZnO@ZIF-8 nanorods, the photocatalytic degradation rate reached 99.4% after 4.5 min, which is more than twice that obtained using bare ZnO nanorods. Video S1† shows the MB degradation by the ZnO@ZIF-8 nanocomposites. Within 3 min, the color of the MB aqueous solution became visibly lighter. This result indicates that ZnO@ZIF-8 exhibits outstanding photocatalytic activity under solar light, which is better than most ZnO-based catalysts reported in the literature (Table S1†).

Furthermore, Table S1† lists the photocatalytic degradation performances of some ZnO-based materials for comparison. Although these results reported in the literature were mostly obtained under UV irradiation, the improvement of the efficiency of the photocatalysts prepared by them is still limited. However, in the present study, the photocatalytic process was conducted under solar light and MB was almost completely degraded within 4.5 min, demonstrating the significant improvement in the photocatalytic activity attained using the proposed ZnO@ZIF-8 core–shell heterostructures. Fig. 5c and S3d† show $\ln(C_0/C)$ as a function of the reaction time for MB photocatalytic degradation, for various photocatalyst nanoparticles. In many cases, the photocatalytic degradation of MB obeys a first-order kinetic equation, like the following pseudo-first-order equation.

$$\ln(C_0/C) = kt, \tag{2}$$

where k (in min^{-1}) is the degradation rate constant and t (in min) is the reaction time. The photocatalytic activity of the samples was evaluated based on k (Fig. 5c and S3d†), that is, the higher the k value, the higher the photocatalytic activity. The k value of the ZnO@ZIF-8 nanocomposites (1.0310 min^{-1}) was bigger than those of the ZnO nanorods (0.3728 min^{-1}) and ZIF-8 (0.0133 min^{-1}), demonstrating that ZIF-8 promotes the photocatalysis by ZnO. To test the stability of
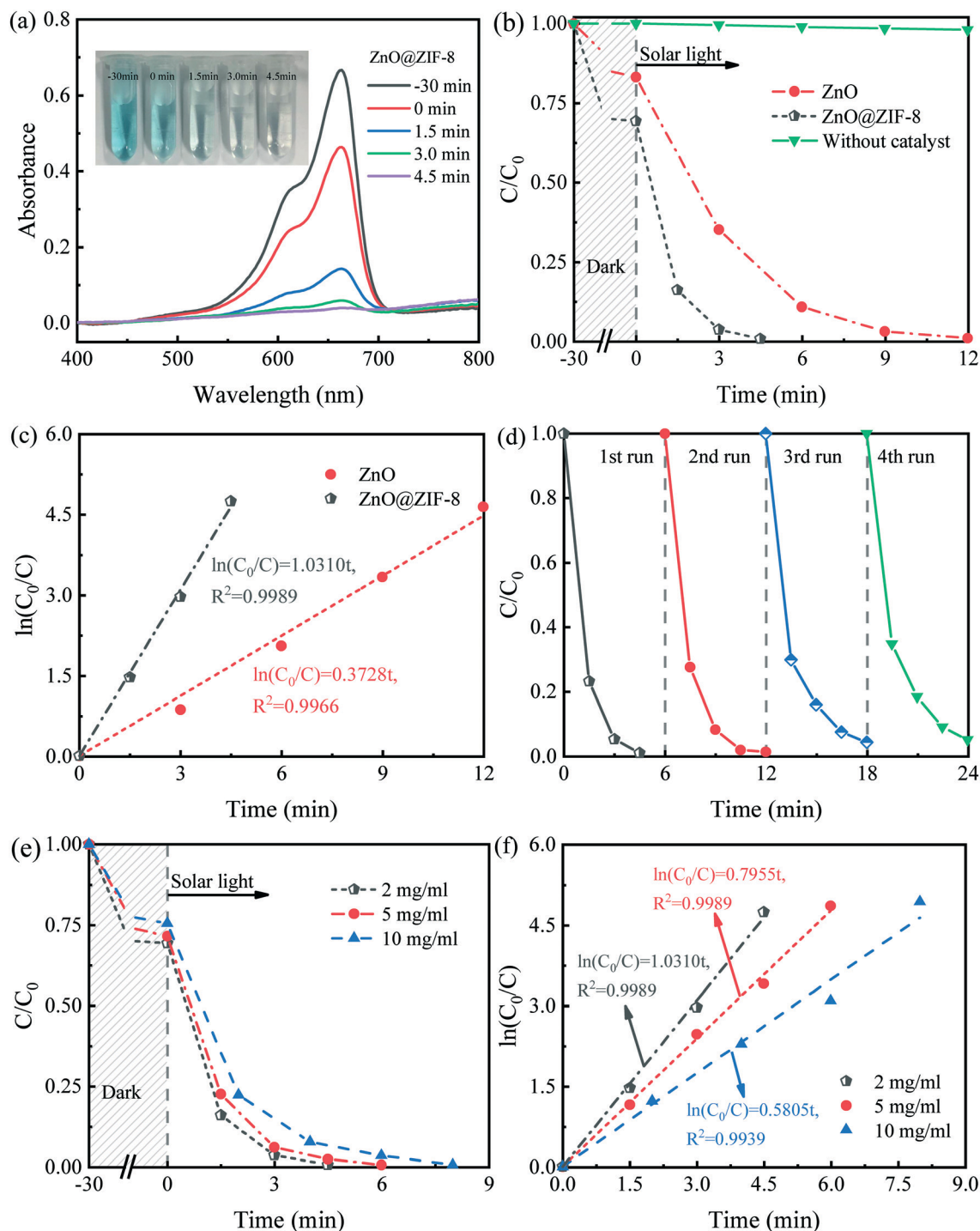
Fig. 5 Time-dependent UV-vis absorption spectra for the methylene blue (MB) degradation using (a) ZnO@ZIF-8 photocatalyst under natural light (inset in (a) shows photographs of color change of the photodegradation reaction solution). (b) Photocatalytic degradation of MB in aqueous solution using different photocatalyst nanoparticles. (c) Plots of $\ln(C_0/C)$ *vs.* reaction time for the MB photocatalytic degradation using various photocatalyst nanoparticles. (d) Photocatalytic stability test of the ZnO@ZIF-8 photocatalyst under natural light. (e) Degradation curve of ZnO@ZIF-8 under natural light prepared by various concentrations of 2-MeIm ethanol solution. (f) Plots of $\ln(C_0/C)$ *vs.* reaction time for the MB photocatalytic degradation using various photocatalyst nanoparticles. 50 mg of the photocatalyst was added to 50 mL of 1.0×10^{-5} M MB aqueous solution.

the photocatalytic activity of the ZnO@ZIF-8 nanorods, the photocatalyst was separated *via* centrifugation after the photocatalytic reaction and reused for other

photodegradation cycles. After 4 cycles, 95% of the MB photodegradation rate was maintained (Fig. 5d), indicating good photocatalytic stability. The XRD pattern of ZnO@ZIF-8

(Fig. S4†) also shows no obvious change after the cycling experiment, suggesting excellent stability. Fig. S5† shows the photocatalytic degradation of Rhodamine B (RhB) using ZnO@ZIF-8 and ZnO nanorods as the photocatalysts under solar light. The results showed that RhB was almost completely degraded by ZnO@ZIF-8 in 45 min, indicating that ZnO@ZIF-8 has excellent photocatalytic activity and is significantly higher than ZnO.

Fig. 5e and f compare the photocatalytic degradation results obtained using the ZnO@ZIF-8 nanorods that were prepared with various 2-Melm concentrations, showing that increasing the 2-Melm concentration reduced the photodegradation efficiency of the resulting photocatalyst. Besides, the k value was 1.0310, 0.7955, and 0.5805 min^{-1} for the 2-Melm concentration of 2, 5, and 10 mg mL^{-1}, respectively. When the 2-Melm concentration was 10 mg mL^{-1}, the corresponding photocatalyst took at least 8 min to completely degrade MB. This may be closely related to the thickness of the ZIF-8 shell formed on the ZnO nanorod surface and the formation of ZIF-8 nanoparticles. As reported by Wang et al.,[19] in ZnO@ZIF-8 nanocomposites, the ZIF-8 layer thickness increases along with the 2-Melm concentration, and this thickness increase can improve the specific surface area of the photocatalyst, enhancing its adsorption performance. However, the excessive thickness of the shell hinders the light absorption by the ZnO core due to the weak light absorption by the ZIF-8 layer. During the separation and transfer of the photogenerated charges, whether the photogenerated charges can quickly reach the photocatalyst surface determines whether it can participate in the photocatalytic reaction, and the charge transfer usually depends on the structure and surface morphology of the semiconductor.[43] Table S2† lists the core (ZnO) diameters and shell (ZIF-8) thicknesses of various ZnO@ZIF-8 nanocomposites reported in previous studies, showing that all shells are too thick (>30 nm) to promote the photocatalytic activity. The photodegradation performance of the photocatalyst benefits from the excitation by light irradiation. Thus, the blocking effect of the shell thickness increase is greater than the promoting effect, reducing the overall photodegradation. Besides, due to the increase of the 2-Melm concentration, the formation of more ZIF-8 nanoparticles that are hard to be excited by solar light irradiation also reduces the photocatalytic ability.

Possible photocatalytic mechanism

The ZnO@ZIF-8 core–shell heterostructures prepared using the three above-mentioned 2-Melm concentrations all showed excellent photocatalytic activity. Even the smallest k value among them (0.5805 min^{-1}), obtained with the 2-Melm concentration of 10 mg mL^{-1}, was bigger than that of bare ZnO nanorods (0.3728 min^{-1}). This indicates that the strategy of combining ZIF-8 with ZnO nanorods significantly improved the photocatalytic activity of ZnO. Some researchers attributed the improvement of the photocatalytic properties

of ZnO@ZIF-8 composites to the bandgap decrease.[19,36] However, the specific bandgap data listed in Table S3† show that there was no significant decrement in the ZnO bandgap after the formation of the ZIF-8 shell, in contrast, the bandgap of the synthesized ZnO@ZIF-8 nanocomposites was even slightly larger than that of the bare ZnO nanorods. As shown in the UV-vis absorption spectra of the synthesized materials (Fig. S6a†), both the ZnO and ZnO@ZIF-8 nanocomposites absorbed in the wavelength range of 200–400 nm. The bandgap values derived from these spectra were 3.12 and 3.17 eV for the ZnO and ZnO@ZIF-8 nanorods, respectively (Fig. S6b†). Li et al.[33] reported that introducing ZIF-8 on the surface of ZnO nanocomposites would increase their bandgap due to larger bandgap of ZIF-8.

Fig. S7† shows the electrochemical impedance spectra (EIS) and transient photocurrent response curves of the as-prepared samples. As shown in Fig. S6a and b,† the bare ZnO exhibits the smallest arc radius and the highest photocurrent response intensity, while ZIF-8 shows the opposite results. When ZnO is combined with another one which has relatively higher carrier mobility, such as graphene and Au, the carrier mobility of the composite must be increased.[44] As for ZnO@ZIF-8, when the ZnO semiconductor is combined with ZIF-8, which has relatively lower carrier mobility, the carrier mobility of the composite would be reduced.[34] Thus, the reduction of the photocurrent response of ZnO@ZIF-8 occurred. However, the photocurrent results can only manifest that the bare ZnO possesses the lowest charge transfer resistance, but not verify that it exhibits the highest photocatalytic activity. Many researchers have reported that the photocurrent is not in agreement with the photocatalytic activity.[44,45]

Therefore, the possible photocatalytic mechanism of ZnO@ZIF-8 involved can be discussed as follows. Firstly, the core–shell heterostructures prepared in the present study improved the enrichment of MB on the surface of the catalyst. It is worth underlining that the close proximity of MB to the ZnO surface via adsorption will easily cause a photosensitization degradation mechanism (Fig. S6c†). Although the MB molecules have a minimum cross-section size of 8 Å and cannot go through the aperture of ZIF-8 frameworks (3.4 Å),[19] the grain boundaries are an unavoidable microstructural feature in the intergrown polycrystalline ZIF-8 shell structure.[46–48] MB molecules that are too large to go through the channel of ZIF-8 may be able to permeate through the larger inter-crystalline gaps and directly adsorbed on the ZnO surface.[49] In addition, since the ZIF-8 layer is ultra-thin (2–3 nm), the photogenerated electrons generated by photosensitization may be injected into the conduction band of ZnO through the ZIF-8 layer due to the quantum tunneling effect,[50,51] thereby promoting the photodegradation of MB. Secondly, the recombination of the photogenerated electron–hole pairs plays a key role in the photocatalytic activity. Tuncel et al.[36] reported that the synergy between ZnO and ZIF-8 is beneficial to the interfacial charge transfer. Yu et al.[35] attributed the photocatalytic mechanism of ZIF-8 in ZnO@ZIF-8 core–shell composites to

the ligand-to-metal charge transfer where electrons transfer from photoexcited organic ligands to metals under UV irradiation. In terms of photocatalytic activity, ZIF-8 has an absorption edge at ~227 nm and a wide bandgap,[36,52] meaning that its photogenerated electrons can be excited only under UV irradiation.[52,53] In the present work, the photocatalytic degradation of an MB aqueous solution was conducted under solar light, and the synthesized photocatalysts still exhibited excellent photocatalytic performance. It can be inferred that the ultraviolet light in solar light would excite the ZIF-8 shell around the ZnO nanocomposites (Fig. S6d†), the electrons exited from the CB of ZIF-8 would migrate into the CB of ZnO and transform O_2 to $\cdot O^{2-}$. Meanwhile, the holes of ZnO would transfer to the VB of ZIF-8 and convert H_2O to $\cdot OH$.[39,54,55] Thus, the dye was degraded by the active groups with strong oxidation ability successfully. Last but not least, the photocorrosion process would destroy the crystal structure of ZnO and weaken the photostability of the bare ZnO.[56] After introduction of the ZIF-8 shell, the photogenerated holes on ZnO could transfer to ZIF-8, and then inhibit photocorrosion and reduce the defects on the ZnO nanocomposite surface.[33,57]

Conclusions

ZnO@ZIF-8 core–shell nanorods were prepared through the direct reaction of ZnO nanorods with 2-methylimidazole, without adding any other zinc salt, by taking advantage of the high specific surface area of MOFs and using ZnO nanorods as the zinc source. The photocatalytic activity of the synthesized ZnO@ZIF-8 nanocomposites was tremendously improved, which is significantly higher than that of the similar ZnO-based composites reported and could completely degrade MB in ~4.5 min under solar light irradiation. Besides, the nanocomposites exhibited high stability after four cycles. This study highlights a promising approach for effectively improving the photocatalytic activity of ZnO semiconductors.

Conflicts of interest

The authors have declared no conflict of interest.

Acknowledgements

References

1 S. K. Loeb, P. J. J. Alvarez, J. A. Brame, E. L. Cates, W. Choi, J. Crittenden, D. D. Dionysiou, Q. Li, G. Li-Puma, X. Quan, D. L. Sedlak, T. David Waite, P. Westerhoff and J. H. Kim, *Environ. Sci. Technol.*, 2019, **53**, 2937–2947.

2 T. T. Nguyen, S. N. Nam, J. Kim and J. Oh, *Sci. Rep.*, 2020, **10**, 13090.

3 M. Pirhashemi, A. Habibi-Yangjeh and S. Rahim Pouran, *J. Ind. Eng. Chem.*, 2018, **62**, 1–25.

4 J. N. Schrauben, R. Hayoun, C. N. Valdez, M. Braten, L. Fridley and J. M. Mayer, *Science*, 2012, **336**, 1298–1301.

5 K. Wetchakun, N. Wetchakun and S. Sakulsermsuk, *J. Ind. Eng. Chem.*, 2019, **71**, 19–49.

6 C. Tian, Q. Zhang, A. Wu, M. Jiang, Z. Liang, B. Jiang and H. Fu, *Chem. Commun.*, 2012, **48**, 2858–2860.

7 C. Hariharan, *Appl. Catal., A*, 2006, **304**, 55–61.

8 R. A. Palominos, M. A. Mondaca, A. Giraldo, G. Peñuela, M. Pérez-Moya and H. D. Mansilla, *Catal. Today*, 2009, **144**, 100–105.

9 J. Wang, Y. Xia, Y. Dong, R. Chen, L. Xiang and S. Komarneni, *Appl. Catal., B*, 2016, **192**, 8–16.

10 Q. Chen, H. Wang, Q. Luan, R. Duan, X. Cao, Y. Fang, D. Ma, R. Guan and X. Hu, *J. Hazard. Mater.*, 2020, **385**, 121527.

11 Y. Jing, J. Wang, B. Yu, J. Lun, Y. Cheng, B. Xiong, Q. Lei, Y. Yang, L. Chen and M. Zhao, *RSC Adv.*, 2017, **7**, 42030–42035.

12 J. Xu, M. Li, L. Yang, J. Qiu, Q. Chen, X. Zhang, Y. Feng and J. Yao, *Chem. Eng. J.*, 2020, **394**, 125050.

13 H. J. Jung, R. Koutavarapu, S. Lee, J. H. Kim, H. C. Choi and M. Y. Choi, *J. Alloys Compd.*, 2018, **735**, 2058–2066.

14 J. Yang, J. Wang, X. Li, D. Wang and H. Song, *Catal. Sci. Technol.*, 2016, **6**, 4525–4534.

15 Z. B. Yu, Y. P. Xie, G. Liu, G. Q. Lu, X. L. Ma and H. M. Cheng, *J. Mater. Chem. A*, 2013, **1**, 2773–2776.

16 L. H. Yu, W. Chen, D. Z. Li, J. B. Wang, Y. Shao, M. He, P. Wang and X. Z. Zheng, *Appl. Catal., B*, 2015, **164**, 453–461.

17 A. Serrà, Y. Zhang, B. Sepúlveda, E. Gómez, J. Nogués, J. Michler and L. Philippe, *Water Res.*, 2020, **169**, 115210.

18 G. Ren, Z. Li, W. Yang, M. Faheem, J. Xing, X. Zou, Q. Pan, G. Zhu and Y. Du, *Sens. Actuators, B*, 2019, **284**, 421–427.

19 X. B. Wang, J. Liu, S. Leong, X. C. Lin, J. Wei, B. Kong, Y. Xu, Z. X. Low, J. F. Yao and H. T. Wang, *ACS Appl. Mater. Interfaces*, 2016, **8**, 9080–9087.

20 X. M. Cao and Z. B. Han, *Chem. Commun.*, 2019, **55**, 1746–1749.

21 X. Zeng, L. Huang, C. Wang, J. Wang, J. Li and X. Luo, *ACS Appl. Mater. Interfaces*, 2016, **8**, 20274–20282.

22 M. R. Di Nunzio, E. Caballero-Mancebo, B. Cohen and A. Douhal, *J. Photochem. Photobiol., C*, 2020, **44**, 100355.

23 F. Tian, A. M. Cerro, A. M. Mosier, H. K. Wayment-Steele, R. S. Shine, A. Park, E. R. Webster, L. E. Johnson, M. S. Johal and L. Benz, *J. Phys. Chem. C*, 2014, **118**, 14449–14456.

24 J. Cravillon, S. Münzer, S. J. Lohmeier, A. Feldhoff, K. Huber and M. Wiebcke, *Chem. Mater.*, 2009, **21**, 1410–1412.

25 W. Xia, A. Mahmood and R. Zou, *Energy Environ. Sci.*, 2015, **8**, 1837–1866.

26 A. G. Slater and A. I. Cooper, *Science*, 2015, **348**, 8075.

27 H. Furukawa, K. E. Cordova, M. O'Keeffe and O. M. Yaghi, *Science*, 2013, **341**, 6149–6160.

28 C. C. Wang, J. R. Li and X. L. Lv, *Energy Environ. Sci.*, 2014, **7**, 2831–2867.

29 A. Brown, N. Brunelli, K. Eum, F. Rashidi, J. Johnson, W. Koros, C. W. Jones and S. Nair, *Science*, 2014, **345**, 72–75.

30 H. P. Jing, C. C. Wang, Y. W. Zhang, P. Wang and R. Li, *RSC Adv.*, 2014, **4**, 54454–54462.

31 Y. Ma, X. Wang, X. Sun, T. Wang, Y. Liu, Q. Huo, S. Song and Z. A. Qiao, *Inorg. Chem. Front.*, 2020, **7**, 1046–1053.

32 S. S. Nair, N. Illyaskutty, B. Tam, A. O. Yazaydin, K. Emmerich, A. Steudel, T. Hashem, L. Schöttner, C. Wöll, H. Kohler and H. Gliemann, *Sens. Actuators, B*, 2020, **304**, 127184.

33 Y. Li, S. Xiao, W. Li, X. He, W. Fang, H. Chen, J. Ge and L. Zhao, *JMatS*, 2020, vol. 55, pp. 7453–7463.

34 W. W. Zhan, Q. Kuang, J. Z. Zhou, X. J. Kong, Z. X. Xie and L. S. Zheng, *J. Am. Chem. Soc.*, 2013, **135**, 1926–1933.

35 B. Yu, F. Wang, W. Dong, J. Hou, P. Lu and J. Gong, *Mater. Lett.*, 2015, **156**, 50–53.

36 D. Tuncel and A. N. Ökte, *Catal. Today*, 2020, **361**, 191–197.

37 Y. Guo, X. Cao, X. Lan, C. Zhao, X. Xue and Y. Song, *J. Phys. Chem. C*, 2008, **112**, 8832–8838.

38 J. J. Rueda-Marquez, I. Levchuk, P. Fernández Ibañez and M. Sillanpää, *J. Cleaner Prod.*, 2020, **258**, 120694.

39 W. L. Zhong, C. Li, X. M. Liu, X. K. Bai, G. S. Zhang and C. X. Lei, *Microporous Mesoporous Mater.*, 2020, **306**, 110401.

40 Y. Guo, H. Wang and C. He, *Langmuir*, 2009, **25**, 4678–4684.

41 K. Rajeshwar, M. E. Osugi, W. Chanmanee, C. R. Chenthamarakshan, M. V. B. Zanoni, P. Kajitvichyanukul and R. Krishnan-Ayer, *J. Photochem. Photobiol., C*, 2008, **9**, 171–192.

42 S. K. Lee, A. Mills and N. Wells, *Catal. Today*, 2018, **313**, 211–217.

43 G. Tian, Y. Chen, W. Zhou, K. Pan, C. Tian, X. R. Huang and H. Fu, *CrystEngComm*, 2011, **13**, 2994–3000.

44 Y. Liu, C. Xie, J. Li, T. Zou and D. Zeng, *Appl. Catal., A*, 2012, **433–434**, 81–87.

45 C. Li, J. Zhang, J. A. Yang, T. Wang, X. Lv and Z. Tang, *Appl. Catal., A*, 2011, **402**, 80–86.

46 Y. Li, L. Li, L. Zhu, L. Gu and X. Cao, *Chem. Commun.*, 2016, **52**, 5520–5522.

47 Y. Li, M. Chen, M. Chu, X. Wang, Y. Wang, X. Lin and X. Cao, *ChemElectroChem*, 2021, **8**, 829–838.

48 C. Chen, A. Ozcan, A. O. Yazaydin and B. P. Ladewig, *J. Membr. Sci.*, 2019, **575**, 209–216.

49 M. R. Abdul Hamid and H.-K. Jeong, *J. Ind. Eng. Chem.*, 2020, **88**, 319–327.

50 D. Wang, J. Huang, Y. Lei, W. Fu, Y. Wang, P. Deng, H. Cai and J. Liu, *Opt. Express*, 2019, **27**, 14344–14352.

51 D. Zhang, Z. Zhang, W. Jiang, Y. Gao and Z. Wang, *Nanoscale*, 2018, **10**, 18622–18626.

52 H. P. Jing, C. C. Wang, Y. W. Zhang, P. Wang and R. Li, *RSC Adv.*, 2014, **4**, 54454–54462.

53 L. Wee, N. Janssens, S. Sree, C. Wiktor, E. Gobechiya, R. Fischer, C. Kirschhock and J. Martens, *Nanoscale*, 2014, **6**, 2056–2060.

54 M. A. Nasalevich, M. V. D. Veen, F. Kapteijn and J. Gascon, *CrystEngComm*, 2014, **16**, 4919–4926.

55 M. Chin, C. Cisneros, S. M. Araiza, K. M. Vargas, K. M. Ishihara and F. Tian, *RSC Adv.*, 2018, **8**, 26987–26997.

56 Y. Wang, R. Shi, J. Lin and Y. Zhu, *Energy Environ. Sci.*, 2011, **4**, 2922–2929.

57 H. Kim, W. Kim, J. Park, N. Lim, R. Lee, S. J. Cho, Y. Kumaresan, M. K. Oh and G. Y. Jung, *Nanoscale*, 2018, **10**, 21168–21177.